SUPPLEMENTARY MATERIALS for L. Y. Chen et al.,
"Conditional Deletion of All Neurexins Defines Range of Essential Synaptic Organizer Functions for Neurexins"
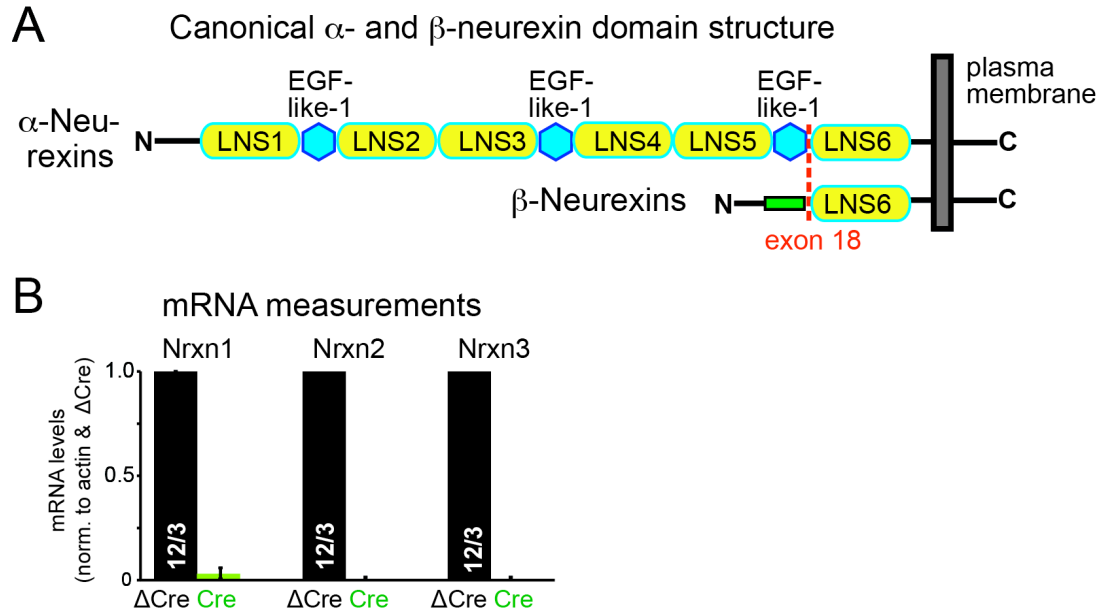
SUPPLEMENTARY FIGURES and FIGURE LEGENDS

Figure S1: **Design and validation of triple Nrxn123 cKO mice that allow conditional deletion of all α- and β-neurexins** (related to all figures)

(A) Diagram illustrating canonical α- and β-neurexin domain structures (LNS = laminin/neurexin/sex-hormone binding globulin domain; signal peptides are not shown). The first exon that is shared by all α- and β-neurexin transcripts (exon 18 in Nrxn1, indicated in red) is indicated; this is the exon that was flanked by loxP sites for all three mouse neurexin genes to generate the triple Nrxn123 cKO mice. The individual floxed Nrxn3 cKO mice were previously published (Aoto et al., 2015); individual Nrxn1 and Nrxn2 cKO mice will be characterized and published separately later.

(B) Quantitative RT-PCR measurements of Nrxn1, Nrxn2, and Nrxn3 mRNA transcripts in cultured hippocampal neurons to demonstrate that Cre-recombinase induces a full deletion of all neurexins in the neurons harboring the six floxed alleles of the triple Nrxn123 cKO mice. Cultured neurons from triple Nrxn123 cKO mice were infected at days in vitro (DIV) 4 with lentiviruses expressing mutant inactive Cre-recombinase (ΔCre, as control) or wild-type active Cre-recombinase (Cre), then collected and analyzed at DIV 14 by RT-PCR with primers spanning the deleted exon. Data are means ± SEMs; numbers in bars indicate sample numbers of cultured hippocampal neurons collected from three independent blinded experiments.

A — Analysis of cerebellar climbing-fiber synapses

Homozygous Nrxn123 cKO

Sparse inferior olive infection:
Control: AAV-CAG-mVenus-p2A-ΔCre
Test: AAV-CAG-double floxed EGFP + Lenti-syn-Cre

Global inferior olive infection:
Control: AAV-CAG-mVenus-p2A-ΔCre
Test: AAV-CAG-double floxed EGFP + AAV-syn-Cre

B — Analysis of synapses formed by Pv- and SST-positive interneurons in the medial prefrontal cortex

Homozygous Nrxn123 cKO

X Pv-Cre mice

Perisomatic inhibition
Pv
Pv
Control: Pv-Cre or Nrxn123 cKO
Test: Nrxn123 cKO/Pv-Cre

X SST-Cre mice

Dendritic inhibition
SST
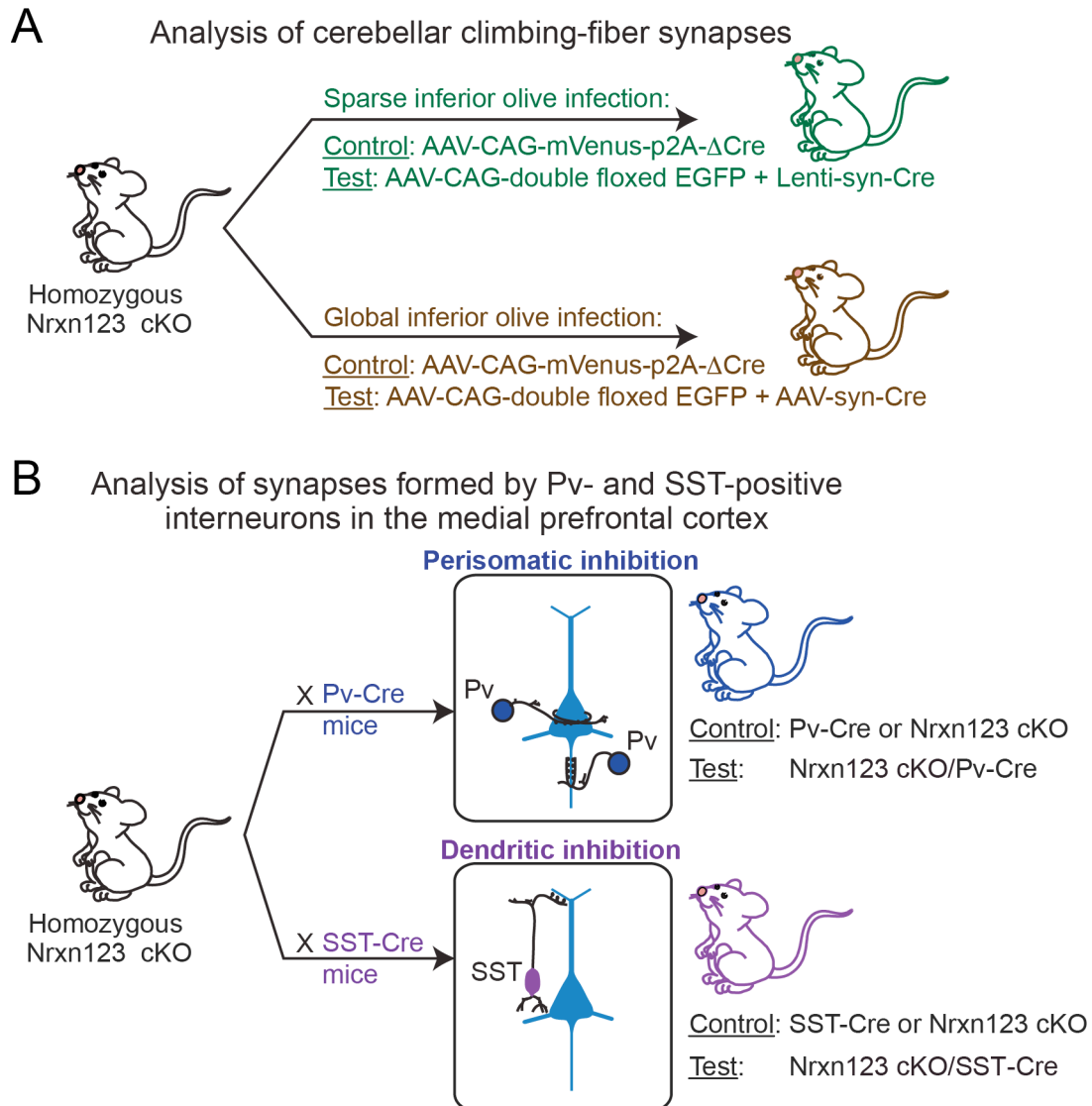Control: SST-Cre or Nrxn123 cKO
Test: Nrxn123 cKO/SST-Cre

Figure S2: **Experimental design for the analysis of the effect of pan-neurexin deletions in three defined synapses (cerebellar climbing-fiber synapses, and synapses formed by Pv[+]- and SST[+]-interneurons on pyramidal neurons in layer 5 of the mPFC) using triple Nrxn123 cKO mice** (related to all figures)

(A) Strategy for sparse and global deletions of all neurexins in climbing-fiber synapses using in vivo P0 injections of the inferior olivary nucleus with lentiviruses or AAVs, respectively, and analyses of the mice at P24.

(B) Strategy for selective deletions of all neurexins in Pv[+]-interneurons using Pv-Cre mice (top) or in SST[+]-interneurons using SST-Cre mice (bottom). Note that PV^{+} cells mainly mediate perisomatic inhibition in pyramidal cells, whereas SST^{+} cells mediate dendritic inhibition. Mice were analyzed at P35-P40.
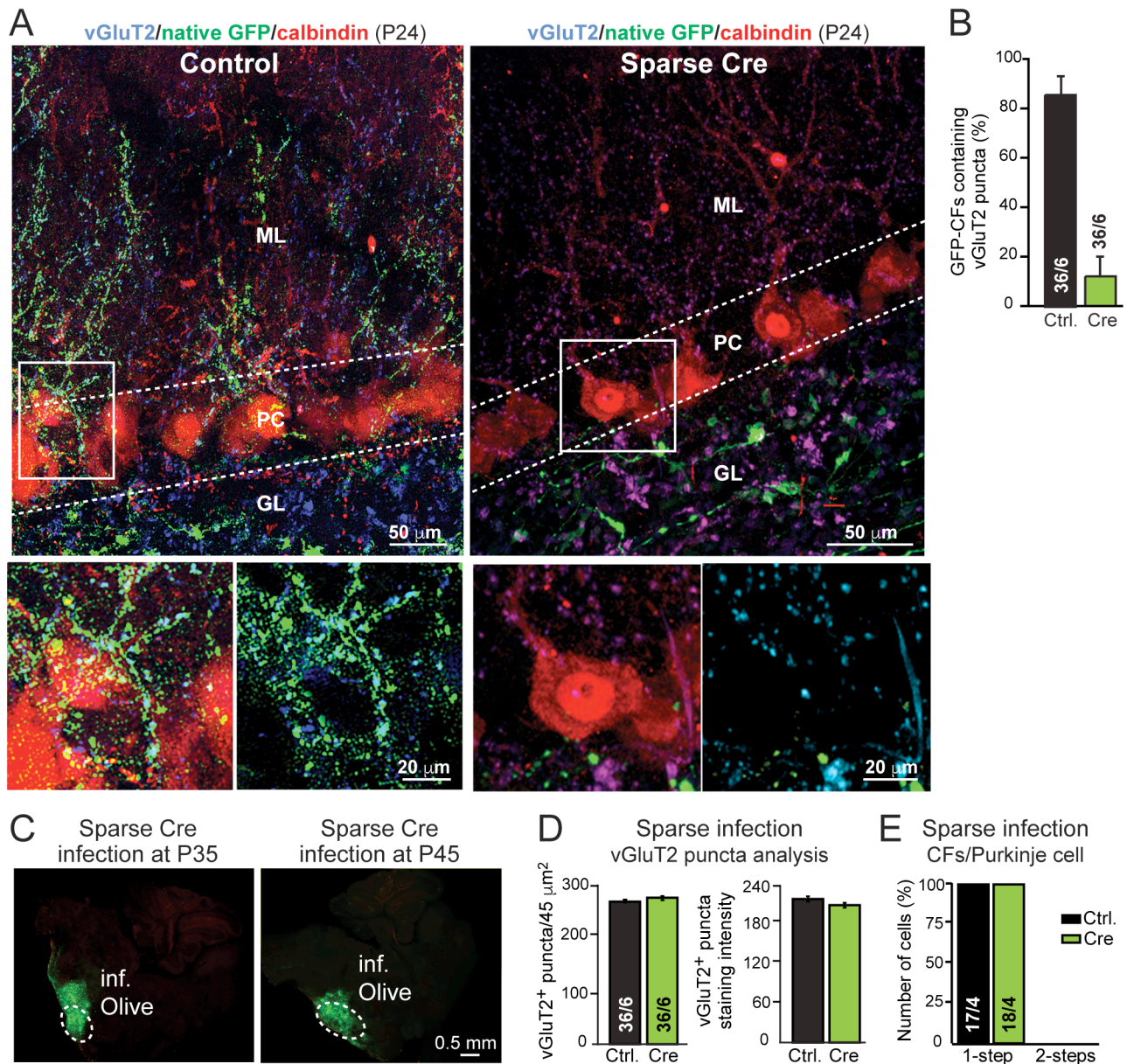
Figure S3: **Analysis of the effect of the sparse pan-neurexin deletion on olivo-cerebellar climbing-fiber axons and synapses** (related to Fig. 1)

(A) Analysis of synapses associated with EGFP-labelled climbing fibers after sparse lentiviral deletions of neurexins in the inferior olive. Images show EGFP-fluorescence of climbing fibers and labeling for vGluT2 to identify climbing fiber-associated synapses and for calbindin to identify Purkinje cells. Top, low magnification images; bottom, higher magnification images corresponding to the boxed area (left: all three colors, right: GFP-CF and vGluT2 only).

(B) Summary graph of the percentage of EGFP-positive climbing fibers containing associated vGluT2-positive puncta near the Purkinje cell soma. Quantifications were performed using Nikon Elements analysis software on 100 μm^2 large regions of interests; double EGFP/vGluT2 labeled objects were scored.

(C) Representative confocal images of sagittal brain sections of cerebellum and brain stem after sparse infection of the inferior olive in Nrxn123 cKO mice with Cre-expressing at P0. Injection sites were confirmed in each animal and sections were collected at P35 (left) or P45 (right).

(D) Additional quantifications of vGluT2-positive puncta in the molecular layer of the cerebellum proximal to Purkinje cells as a function of sparse deletions of neurexins in the inferior olive using lentiviruses (left, summary graph of total puncta density; right, summary graph of vGluT2 puncta staining intensity; complements data in Fig. 1).

(E) Summary graph of the percentage of Purkinje cells exhibiting one or two discrete EPSC amplitudes ("steps") upon increasing the strength of climbing fiber stimulation, as a function of sparse pan-neurexin deletions in the inferior olive and recording from a Purkinje cell adjacent to a climbing fiber from an infected neuron that is identified via its GFP fluorescence.

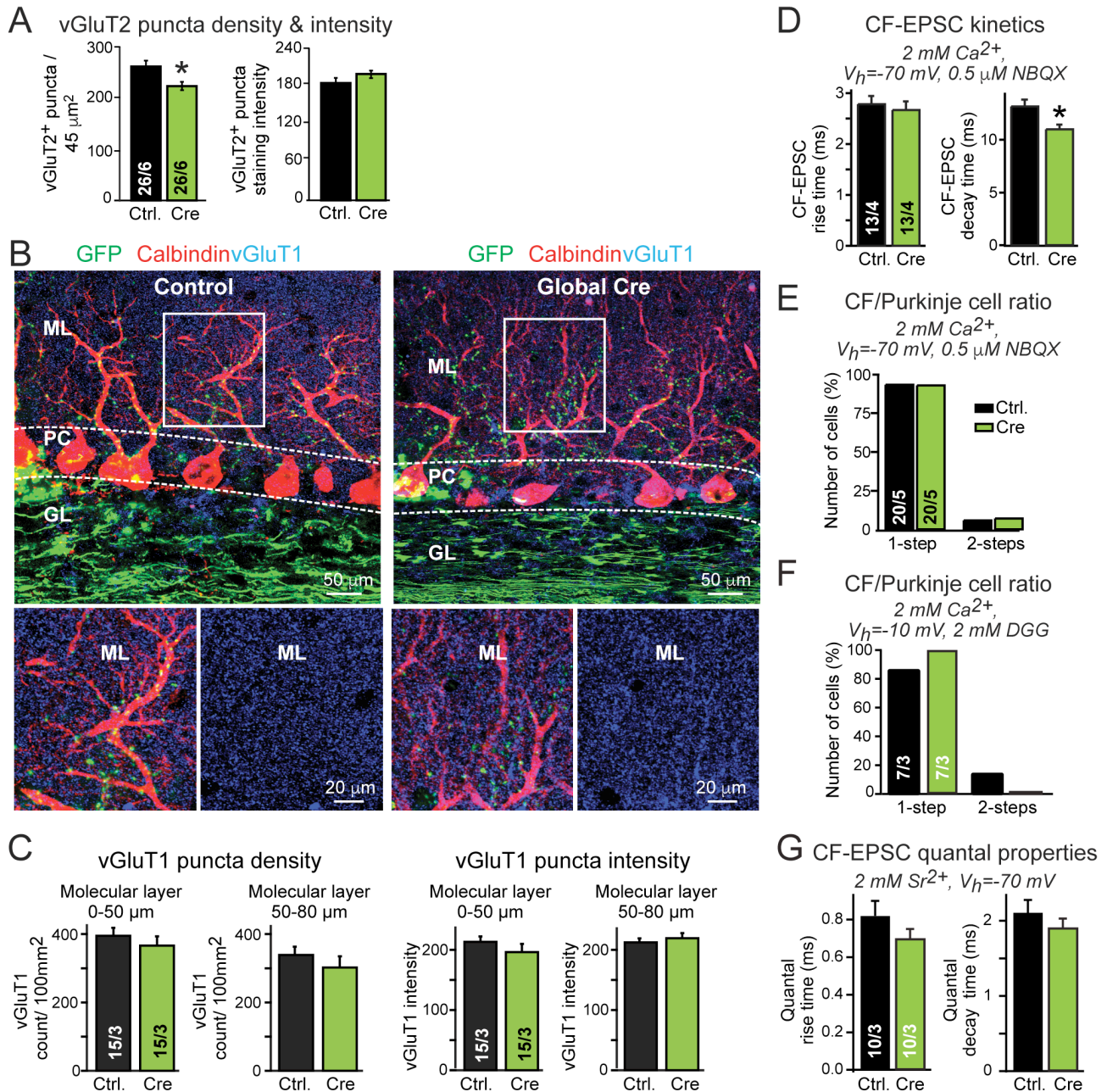Data are means ± SEMs; number of sections/mice (B, D) or cells/mice (E) analyzed are shown in bars.

Figure S4: **Analysis of the effect of global pan-neurexin deletions on olivo-cerebellar climbing-fiber synapses** (related to Fig. 2)

(A) Additional quantifications of vGluT2-positive puncta in the molecular layer of the cerebellum proximal to Purkinje cells as a function of global deletions of neurexins in the inferior olive using AAVs (left, summary graph of total puncta density; right, summary graph of vGluT2 puncta staining intensity).

(B) Representative confocal images of cerebellar cortex sections obtained from mice after global deletions of all neurexins (Nrxn123) in the inferior olive with AAVs expressing mutant (control, left) or active Cre-recombinases (KO, right). Top, low magnification images showing sagittal cerebellar sections with green climbing-fiber fluorescence induced

by AAV-encoded EGFP and immunostaining for calbindin (red) and vGluT1 (blue); bottom, higher magnification images corresponding to the boxed area (left: all three colors, right: vGluT1 only).

(C) Summary graphs of the density (left two graphs) and the intensity (right two graphs) of vGluT1$^+$ synaptic puncta in the molecular layer proximal (0-50 μm) or distal (50-80 μm) to the Purkinje cell layer in cerebella obtained as described in B.

(D) Summary graphs of climbing-fiber EPSC kinetics recorded at P21–P25 after global deletions of neurexins. Recording conditions for the data in this panel and panels E-G are indicated on top.

(**E**) Summary graph depicts percentage of neurons exhibiting a single-step or 2-steps of EPSC response after application of increasingly strong above-threshold stimuli after global deletions of neurexins.

(**F**) Summary graph of the percentage of neurons exhibiting a single-step or 2-steps of EPSC response in the presence of 2 mM DGG after application of increasingly strong above-threshold stimuli after global deletions of neurexins.

(**G**) Summary graphs of quantal event kinetics. Analysis using Sr^{2+} as the divalent cation in the medium instead of Ca^{2+} reveals that quantal kinetics of climbing-fiber synaptic events after global deletions of neurexins are normal.

Data are means ± SEMs; number of sections/mice (A, C) or cells/mice (D-G) analyzed are shown in bars. Statistical significance of controls and neurexin deletions were analyzed by Student's t-test (*, p<0.05; only statistically different comparisons are indicated).

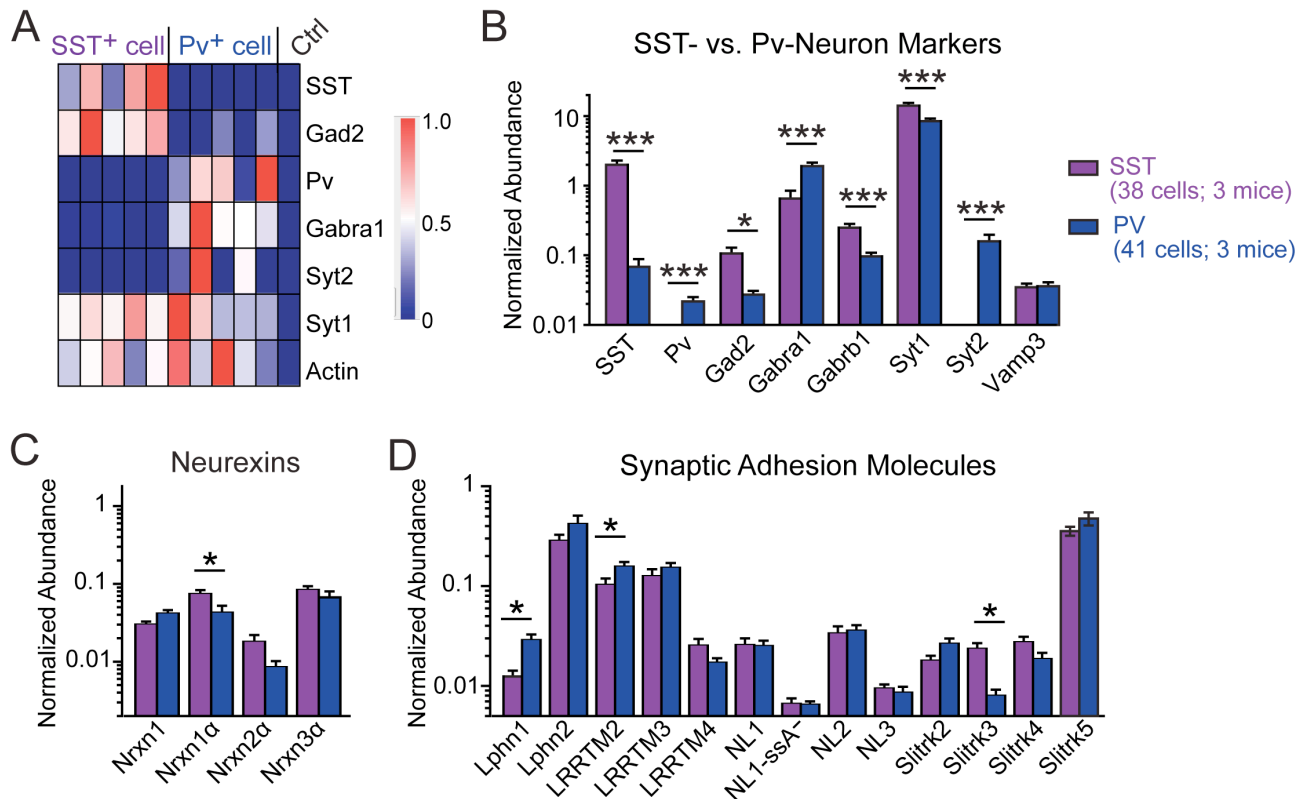Figure S5: **Quantification of mRNA expression levels of marker genes, neurexins, and other synaptic cell-adhesion molecules in individual single Pv$^+$- or SST$^+$-interneurons using fluidigm-based RT-PCR on cytosol aspirated from single patched neurons** (related to Fig. 3-8)

(A) Heatmap image of gene expression patterns in representative Pv$^+$- and SST$^+$-interneurons for molecular markers, synaptotagmin-1 and -2, and actin. Pv$^+$- and SST$^+$-interneurons were identified in acute slice by eYFP fluorescence after viral injections of AAV-EF1α-DIO-eYFP in Pv-Cre and SST-Cre mice, respectively. Mice were stereotactically injected at P21, and analyzed at P35-40.

(B) Average single-cell expression levels of the indicated markers in Pv$^+$- and SST$^+$-interneurons. Normalized abundance of mRNAs was quantified as described in Fuccillo et al. (2015).

(C) Same as B, but for the three principal neurexin genes.

(D) Same as B, but for the indicated synaptic adhesion molecules other than neurexins.

Data are means ± SEM. Asterisks indicate significant differences between Pv$^+$- and SST$^+$-interneurons (Student's t-test). The number of cells and mice analyzed are indicated to the right of graph B, and apply to all graphs. For assay abbreviations and sequence information, see Table S2.
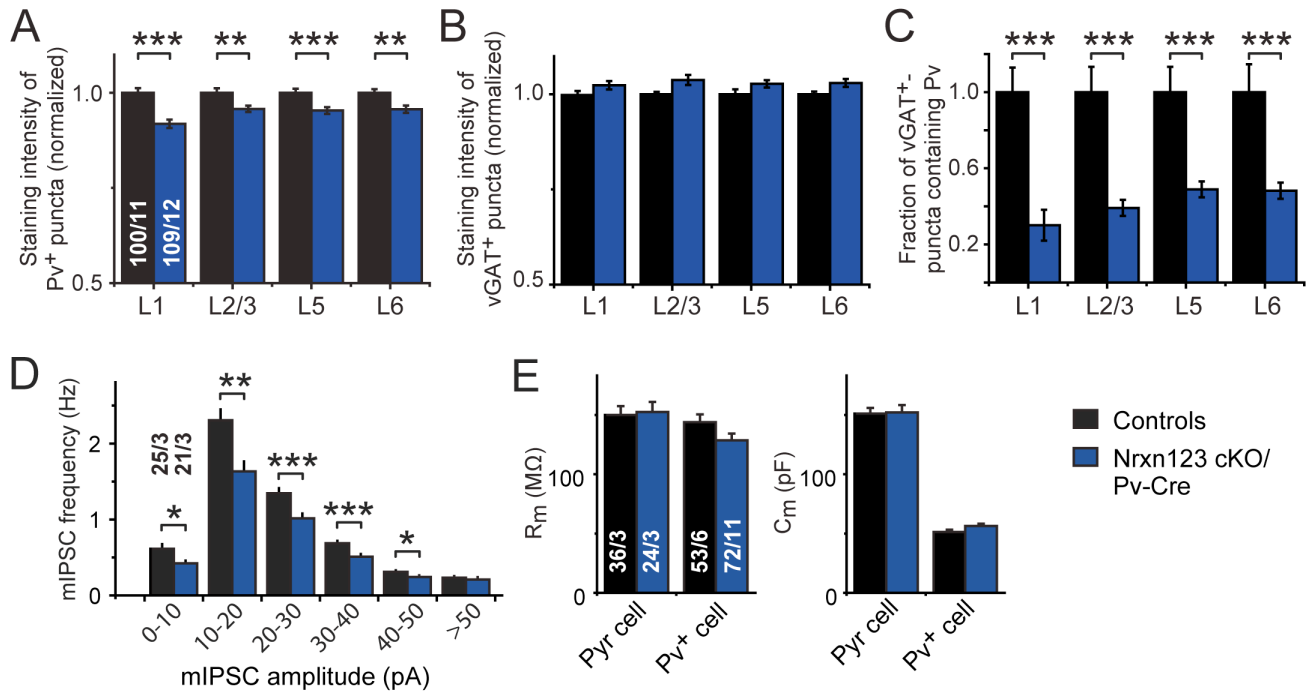
Figure S6: **Summary graphs of additional quantitative parameters for PV⁺ and vGAT⁺ puncta analyzed by immunocytochemistry in various layers of the mPFC in Nrxn123 cKO mice without or with Pv-Cre (A-C), distribution of mIPSC frequencies recorded in acute slices in pyramidal neurons from mPFC layer 5 from Nrxn123 cKO mice without or with Pv-Cre (D), and passive membrane properties of pyramidal and Pv⁺-Cre neurons for the same samples (E)**(related to Fig. 3 and 4).

(A) Summary graph of the parvalbumin staining intensity.

(B) Summary graph of the vGAT staining intensity.

(C) Summary graph of the fraction of vGAT⁺ puncta that are also Pv⁺, thus giving an indication of the fraction of inhibitory synapses that are derived from Pv⁺-interneurons.

(D) Distribution of mIPSC frequencies as a function of mIPSC amplitudes in pyramidal neurons from layer 5 in acute slices from Nrxn123 cKO mice without or with Pv-Cre. All mIPSC events are binned according to the amplitude of individual mIPSC event, and the frequency within each bin was determined by the total number of mIPSC events in the bin divided by the total trial length (300 s). Note that there is a universal reduction of mIPSC frequency independent of quantal amplitude

(E) Summary graph of the membrane resistance (R_m) and capacitance (C_m) of pyramidal (Pyr) cells and Pv⁺ cells in Nrxn123 cKO Pv-Cre mice vs. controls (Nrxn123 cKO for pyramidal neurons; Pv-Cre for Pv⁺ cells). Note that pyramidal cells were monitored with a Cs⁺-based internal pipette solution, whereas Pv⁺- and SST⁺-interneurons were monitored with a K⁺-based internal solution.

Data are means ± SEM. Asterisks indicate significant differences between sections from Nrxn123 cKO without or with Pv-Cre (Student's t-test). For A-C, the number of sections

and mice analyzed are shown in the bar and described in Fig. 3; for D and E, the number of cells/mice analyzed are shown above (D) or in the bars (E).
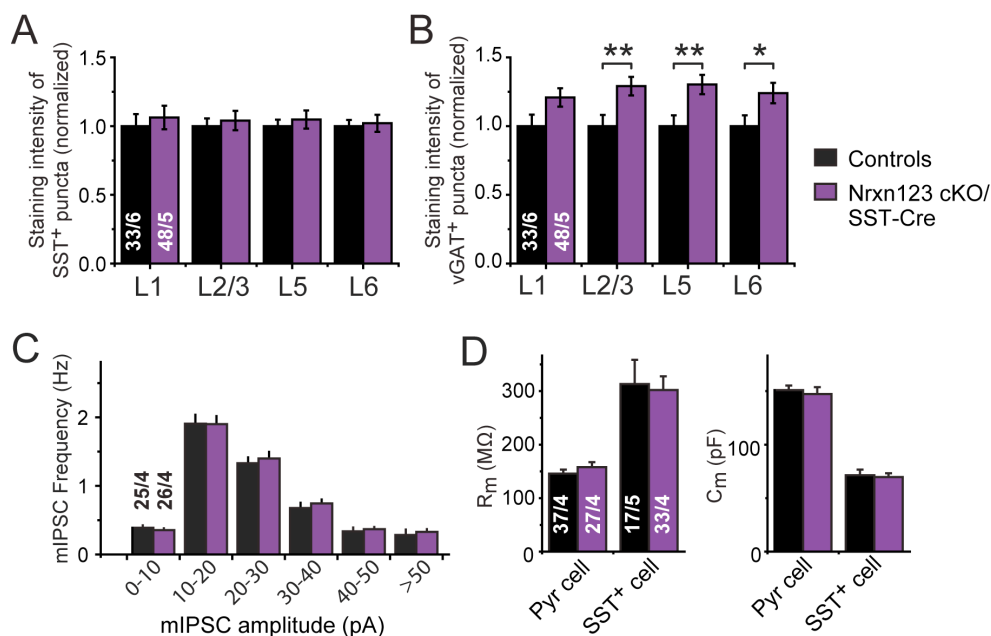
Figure S7: **Summary graphs of additional quantitative parameters for SST⁺ and vGAT⁺ puncta analyzed by immunocytochemistry in all layers of the mPFC Nrxn123 cKO mice without or with SST-Cre (A, B), distribution of mIPSC frequencies recorded in acute slices in pyramidal neurons from mPFC layer 5 from Nrxn123 cKO mice without or with SST-Cre (C), and passive membrane properties of pyramidal neurons and SST⁺-interneurons for the same samples (D)**(related to Fig. 6 and 7)

(A) Summary graph of the somatostatin staining intensity.

(B) Summary graph of the vGAT staining intensity.

(C) Distribution of mIPSC frequencies as a function of mIPSC amplitudes in pyramidal neurons from layer 5 in acute slices from Nrxn123 cKO mice without or with SST-Cre. All mIPSC events are binned according to the amplitude of individual mIPSC event, and the frequency within each bin was determined by the total number of mIPSC events in the bin divided by the total trial length (300 s). Note that there is no difference between control and SST-Cre cells.

(D) Summary graph of the membrane resistance (Rm) and capacitance (Cm) of pyramidal cells and SST⁺ cells in Nrxn123 cKO SST-Cre mice vs. controls Nrxn123 cKO for pyramidal neurons; SST-Cre for SST⁺ cells).

Data are means ± SEM. Asterisks indicate significant differences between sections from Nrxn123 cKO without or with SST-Cre (Student's t-test; *, $p < 0.05$; **, $p < 0.01$). For A & B, the number of sections and mice analyzed are shown in the bar and described in Fig. 6; for C & D, the number of cells/mice analyzed are shown above (C) or in the bars (D).

SUPPLEMENTARY TABLE 1 (related to Fig. 5 and 8)
Kinetics of synapses formed by Pv$^+$ or SST$^+$ interneurons on pyramidal neurons in layer 5 of the mPFC as revealed by paired recordings

Kinetics	Pv control pair (n = 26/6)	Pv-Nrxn123 cKO pair (n = 47/11)	SST control pair (n = 10/5)	SST-Nrxn123 cKO pair (n = 7/4)
Connection probability	36.3% (32/88 pairs tested)	36.8% (52/141 pairs tested)	25.6% (11/43 pairs tested)	11.5% (7/61 pairs tested)
Failure rate	3.0 ± 1.7%	3.1 ±1.6%	30.5 ± 8.0%	27.1 ±8.6%
Latency (ms)	0.96 ± 0.04	0.97 ± 0.03	1.58 ± 0.10	2.23 ± 0.12 (***)
SD of latency	0.19 ± 0.04	0.24 ± 0.03	0.51 ± 0.06	0.66 ± 0.07
Amplitude (pA)	270 ± 52	152 ± 21 (*)	27.7 ± 4.0	17.1 ± 0.8 (*)
CV of amplitude	0.30 ± 0.03	0.36 ± 0.03	0.33 ± 0.02	0.34 ± 0.04
Rise time (ms)	0.76 ± 0.04	0.82 ± 0.06	1.83 ± 0.23	2.80 ± 0.26(*)
Decay time (ms)	18.3± 0.9	19.4 ± 0.7	17.0± 1.8	20.1 ± 2.4

Student's t-test was performed between control and cKO pairs for Pv$^+$ and SST$^+$ cells as indicated; number of analyzed connected cell pairs/mice are listed in the relevant figures; * $P<0.05$, ** $P<0.01$. Statistically significant pairs are shown in red.